ACS Catalysis

pubs.acs.org/acscatalysis

Research Article

Nanoscale Colocalization of Fluorogenic Probes Reveals the Role of Oxygen Vacancies in the Photocatalytic Activity of Tungsten Oxide Nanowires

Meikun Shen,[#] Tianben Ding,[#] Steven T. Hartman, Fudong Wang, Christina Krucylak, Zheyu Wang, Che Tan, Bo Yin, Rohan Mishra, Matthew D. Lew,* and Bryce Sadtler*

Cite This: *ACS Catal.* 2020, 10, 2088−2099

Read Online

ACCESS | Metrics & More | Article Recommendations | Supporting Information

ABSTRACT: Defect engineering is a strategy that has been widely used to design active semiconductor photocatalysts. However, understanding the role of defects, such as oxygen vacancies, in controlling photocatalytic activity remains a challenge. Here, we report the use of chemically triggered fluorogenic probes to study the spatial distribution of active regions in individual tungsten oxide nanowires using super-resolution fluorescence microscopy. The nanowires show significant heterogeneity along their lengths for the photocatalytic generation of hydroxyl radicals. Through quantitative, coordinate-based colocalization of multiple probe molecules activated by the same nanowires, we demonstrate that the nanoscale regions most active for the photocatalytic generation of hydroxyl radicals also possess a greater concentration of oxygen vacancies. Chemical modifications to remove or block access to surface oxygen vacancies, supported by calculations of binding energies of adsorbates to different surface sites on tungsten oxide, show how these defects control catalytic activity at both the ensemble and single-particle levels. These findings reveal that clusters of oxygen vacancies activate surface-adsorbed water molecules toward photo-oxidation to produce hydroxyl radicals, a critical intermediate in several photocatalytic reactions.

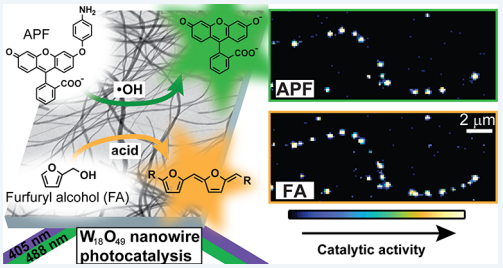

KEYWORDS: *tungsten oxide, oxygen vacancies, fluorescence, single-molecule localization microscopy, colocalization*

INTRODUCTION

Metal oxide semiconductors are promising photocatalysts for a number of important chemical transformations including solar water splitting,[1−6] CO_2 reduction,[6−9] coupling of amines,[10,11] and partial methane oxidation to produce methanol.[12,13] They can be fabricated using inexpensive, solution-phase synthesis, and they are more resistant to corrosion compared to elemental, chalcogenide, and III−V semiconductors. However, as most metal oxides possess electronic band gap energies greater than 2.5 eV, their efficiency is limited by low absorption coefficients where incoming solar radiation is the most intense. Furthermore, due to low electron and hole mobilities, photoexcited charge carriers have a high probability of recombining before they reach the surface to oxidize or reduce adsorbed substrate molecules.[6,14,15] These limitations can be mitigated if the surface of the photocatalyst possesses sites that are highly active for the chemical transformation of interest.

The presence of structural defects, including vacancies, substitutional impurities, and unpassivated atoms, at the surface of a semiconductor can introduce surface states within the band gap that act as recombination centers and deactivate photoexcited charges. However, rather than act as recombination centers, oxygen vacancies appear to enhance catalytic activity in many metal oxide photocatalysts, including tungsten, indium, titanium, molybdenum, and zinc oxide.[3−11,16−20] Several studies have reported higher catalytic activity in these materials as the oxygen vacancy concentration is increased through thermal or chemical treatments, although various mechanisms have been proposed to explain this observation.[3−8,10,11,16] Density functional theory (DFT) calculations suggest that oxygen vacancies act as preferential adsorption sites for reactant molecules and create new states within the electronic band gap of the semiconductor.[4,10] It is currently debated whether or not charge carriers in these localized defect states can participate in photochemical reactions.[4−8,10] Furthermore, the plasmon resonance induced by increased free electron density increases absorption at longer wavelengths.[5,6,21] Currently, there is not a clear consensus as to which of these mechanisms is dominant. A major obstacle in understanding the role oxygen vacancies play in catalytic activity is that different metal oxide particles within a single batch exhibit variations in the concentration and distribution

Received: October 17, 2019
Revised: December 30, 2019
Published: January 8, 2020

https://dx.doi.org/10.1021/acscatal.9b04481
ACS Catal. 2020, 10, 2088−2099

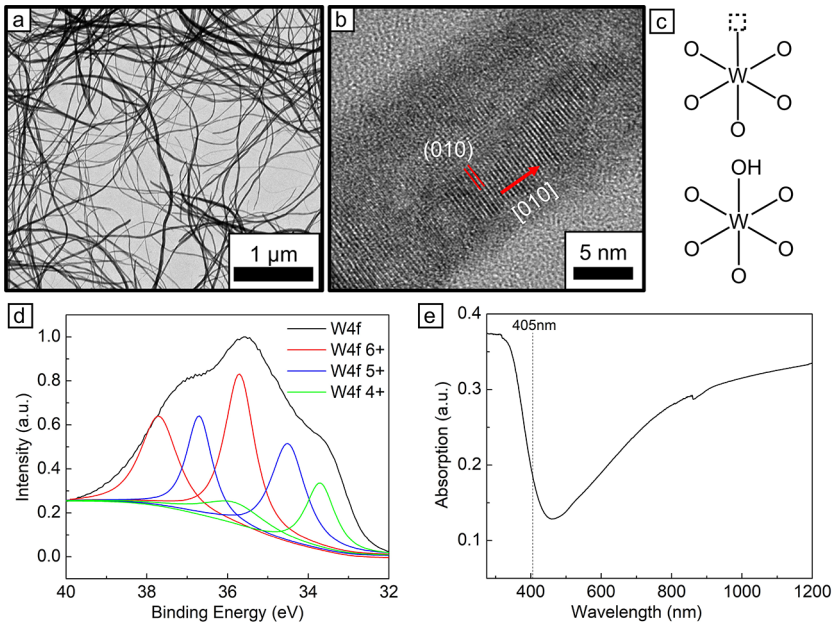

Figure 1. Structural characterization of $W_{18}O_{49}$ nanowires. (a) Low-magnification and (b) high-resolution TEM images of $W_{18}O_{49}$ nanowires. (c) Models for an oxygen vacancy (top) and a hydroxyl group (bottom) at the surface of $W_{18}O_{49}$. (d) X-ray photoelectron spectrum for $W_{18}O_{49}$ nanowires in the binding energy region for W 4f electrons. (e) Absorption spectrum of a dry film of $W_{18}O_{49}$ nanowires.

of oxygen vacancies. This heterogeneity makes it difficult to correlate specific morphological and structural features with catalytic activity when measurements are made on large groups of particles. Thus, methods are needed that can spatially map variations in activity for individual particles and correlate those variations with the specific structural features that lead to high or low activity.

Single-molecule imaging has been applied to study size and shape effects in chemical reactions catalyzed by inorganic nano- and microstructures, including metal nanoparticles,[22−31] layered and mesoporous materials,[31−34] metal oxides,[31,35−40] and metal−metal oxide heterostructures.[31,41,42] By localizing the positions of individual redox-active probe molecules that are chemically triggered by interfacial charge transfer, one can obtain a map of reaction events at the surface of these materials with nanoscale spatial resolution. Several studies have compared electron microscopy and single-molecule fluorescence images of the same catalyst particles to show that their activity can vary along a single-crystal facet or in the regions between groups of closely spaced particles. However, because the spatial resolution provided by this technique (typically 10 to 25 nm) still averages over many atoms on the surface of the catalyst, in most cases, the chemical structure of the active regions could not be conclusively identified.[23−28,36−39]

In this report, we use single-molecule super-resolution imaging of chemically activated molecular probes to map variations in the catalytic activity of tungsten oxide ($W_{18}O_{49}$) nanowires. Activation of the first probe molecule requires photoexcitation above the band gap of the semiconductor to generate hydroxyl radicals. The second reaction does not require photoexcitation but instead relies on the presence of either oxygen vacancies or hydroxyl groups at the surface of the nanowires. Through quantitative colocalization of the spatial distribution of the two probes, we show that the nanowires contain inactive regions dispersed among segments that are catalytically active for both transformations. The high degree of spatial correlation between the two probe reactions enabled us to elucidate the structural nature of the active regions. Segments along each nanowire that contain clusters of oxygen vacancies activate surface-adsorbed water molecules during the photocatalytic generation of hydroxyl radicals, an important intermediate in the production of chemical fuels from sunlight.

RESULTS AND DISCUSSION

Oxygen Vacancies in Tungsten Oxide Nanowires. $W_{18}O_{49}$ nanowires were synthesized using a solvothermal method (see the Supporting Information for further details). An X-ray diffraction pattern of the as-synthesized sample (Figure S1) matched the standard pattern for monoclinic $W_{18}O_{49}$ (PDF card #00-005-0392). Transmission electron microscopy (TEM) images show that the nanowires possess an average diameter of 14 ± 8 nm (average ± 1st standard deviation) and lengths of several micrometers (Figure 1a). A high-resolution TEM (HRTEM) image (Figure 1b) of a section along a single nanowire shows lattice fringes with a spacing of 3.8 Å aligned perpendicular to the nanowire length. This lattice spacing matches the *d*-spacing for the (010) plane of monoclinic $W_{18}O_{49}$, indicating that the nanowire grew along the [010] direction (see Figure S2 for additional HRTEM images).[19,43]

The monoclinic phase of tungsten oxide corresponding to $W_{18}O_{49}$ can accommodate variations in the W:O stoichiometry that arise due to oxygen vacancies.[6,21] Evidence of the presence of oxygen vacancies in the as-synthesized $W_{18}O_{49}$ nanowires was provided by X-ray photoelectron spectroscopy (XPS) (Figure 1d). The W 4f core level peaks obtained by XPS can be assigned to a mixture of W^{6+}, W^{5+}, and W^{4+}.[19,44] Tungsten ions in the +5 and +4 oxidation states compensate the positive charge left by the removal of O^{2-}. We also observe a shoulder peak in the region for O 1s at a higher binding energy than the peak corresponding to lattice oxygen (Figure S3). This peak has been previously attributed to surface-adsorbed oxygen species that bind to metal ions left exposed by oxygen vacancies.[9,11,19] Furthermore, the absorption spectrum of a film

https://dx.doi.org/10.1021/acscatal.9b04481
ACS Catal. 2020, 10, 2088−2099

of $W_{18}O_{49}$ nanowires measured using an integrating sphere shows an absorption edge near 440 nm (Figure 1e), which corresponds to band gap excitation of tungsten oxide (E_g = 2.8 eV). The broad absorption at wavelengths beyond 500 nm has been previously attributed to free carrier absorption induced by surface oxygen vacancies in $W_{18}O_{49}$.[5,6,21] Oxidation of the nanowires using either hydrogen peroxide (H_2O_2) or thermal annealing in air led to the disappearance of free carrier absorption (Figure S4). Oxidation using H_2O_2 preserved the monoclinic $W_{18}O_{49}$ phase of the nanowires (Figure S5), enabling us to compare the catalytic activity of nanowires with and without oxygen vacancies.

Single-Molecule Super-Resolution Imaging. Hydroxyl radicals (·OH) are a key intermediate in several reactions photocatalyzed by metal oxide semiconductors, including water oxidation, the degradation of environmental pollutants, and methane to methanol conversion.[12,13,38,45−47] We hypothesized that differences in the local structure of $W_{18}O_{49}$ nanowires would affect their activity for generating ·OH radicals. To image spatial variations in activity along the length of individual $W_{18}O_{49}$ nanowires, we first chose a fluorogenic probe that is activated in the presence of ·OH radicals (Figure 2b). Cleavage of the aminophenyl group of 3′-(*p*-aminophenyl) fluorescein (APF) by ·OH generates fluorescein.[48] Control experiments using dispersions of $W_{18}O_{49}$ nanowires in solution show that both nanowires containing oxygen vacancies and illumination with photon energies above the band gap of $W_{18}O_{49}$ are needed to induce this reaction at the ensemble level (Figures S13−S16). Individual reaction events for single nanowires dispersed on a glass coverslip were then detected using fluorescence microscopy.

Single-molecule super-resolution microscopy was conducted using total internal reflection fluorescence (TIRF) excitation. In this imaging mode, only fluorophores activated near the surface of the coverslip are detected (Figure 2a).[22−24,37,38] A 405 nm laser coupled into the objective of an inverted microscope was used to excite $W_{18}O_{49}$ nanowires dispersed on a glass coverslip. Simultaneous illumination with a 488 nm laser was used to excite the product fluorescein molecules. After adding a solution of APF (30 nM in a solution of phosphate buffer with pH 7.4), fluorescence intensity bursts were observed (Figure 3a). We attribute these fluorescence bursts to the generation of fluorescein after reaction with photogenerated ·OH radicals adsorbed on the surface of the nanowires. We performed the following control experiments to support this hypothesis. Using APF as a probe, fluorescence signals were not observed on blank coverslips (i.e., without nanowires; Figure S25). Second, fluorescence signals were only observed when using both excitation beams (405 and 488 nm). Furthermore, fluorescence signals were not observed when the reaction was carried out in pure phosphate buffer solution or

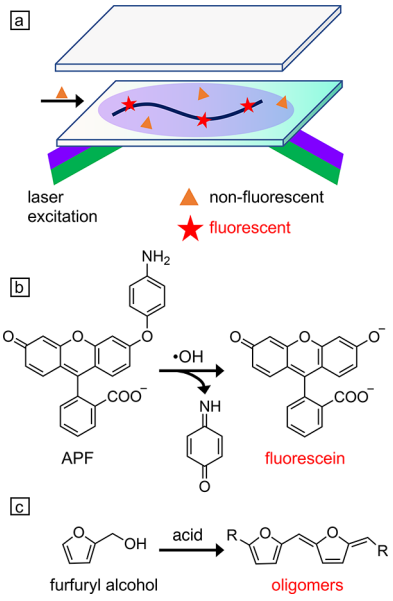

Figure 2. Single-molecule imaging of catalytic reactions using fluorogenic probes. (a) Experimental setup for total internal reflection fluorescence (TIRF) microscopy. One or more lasers are sent through a microscope objective at an angle such that they are internally reflected at a glass coverslip. The $W_{18}O_{49}$ nanowires catalyze the reactions shown in (b) and (c) to convert nonfluorescent substrate molecules (orange triangles) into fluorescent products (red stars). The fluorescence emission is collected through the same objective and imaged by an electron-multiplying CCD camera. (b) Oxidation of 3′-(*p*-aminophenyl) fluorescein (APF) by hydroxyl radicals produces fluorescein. (c) Acid-catalyzed condensation of furfuryl alcohol produces fluorescent oligomers.

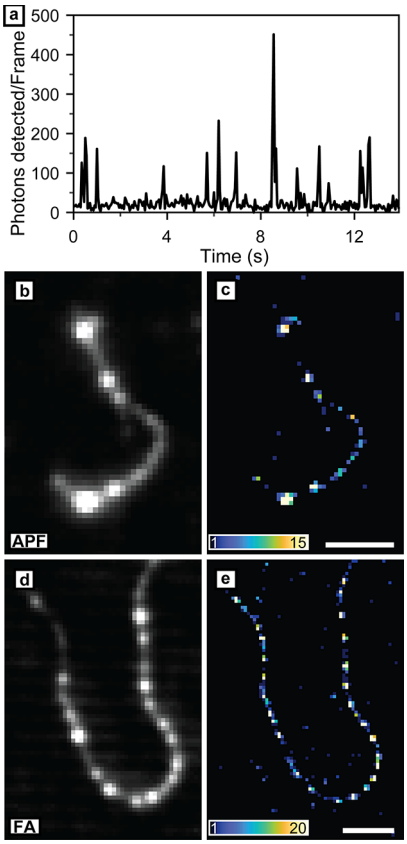

Figure 3. Imaging the catalytic activity of single $W_{18}O_{49}$ nanowires. (a) Trajectory of photons detected in a 1 × 1 μm region for a single $W_{18}O_{49}$ nanowire using APF as a probe molecule. (b) Diffraction-limited image of a $W_{18}O_{49}$ nanowire under the same conditions as in (a). (c) Super-resolution image of the nanowire in (b) containing the positions of all fluorescence bursts. Color scale: number of fluorescence bursts per bin. (d) Diffraction-limited image of a $W_{18}O_{49}$ nanowire using furfuryl alcohol (FA) as a probe molecule. (e) Super-resolution image of the nanowire in (d) containing the positions of all fluorescence bursts. Scale bars: 2 μm.

https://dx.doi.org/10.1021/acscatal.9b04481
ACS Catal. 2020, 10, 2088−2099

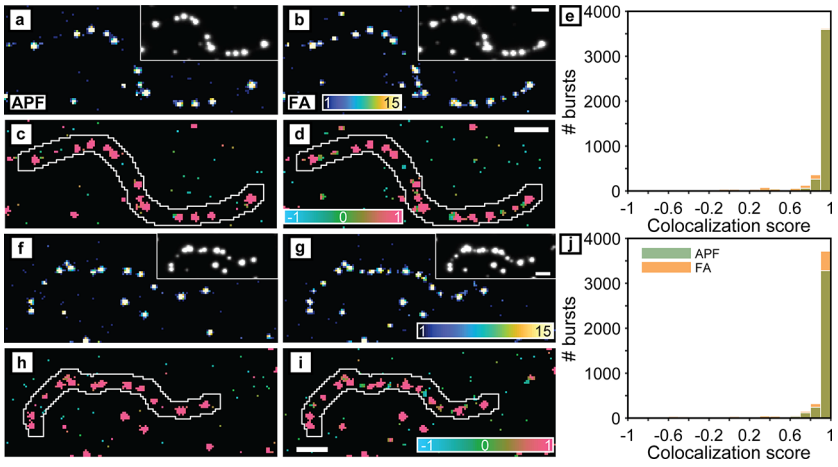

Figure 4. Colocalization of hydroxyl radical generation and Lewis acid sites for two representative $W_{18}O_{49}$ nanowires. Super-resolution images of the initial nanowires using (a, f) APF as a probe to detect hydroxyl radicals and (b, g) furfuryl alcohol (FA) as a probe to identify Lewis acid sites. Color scale: number of fluorescence bursts per bin. Inset: diffraction-limited images of each imaging condition. Coordinate-based colocalization (CBC) of (c, h) APF and (d, i) furfuryl alcohol bursts. Color scale: median colocalization score in each bin ranging from −1 for anticorrelated burst distributions, through 0 for random, to +1 for perfectly correlated burst distributions. White lines depict boundaries of the nanowire regions. All scale bars are 2 μm. The top scale bars apply to the diffraction-limited images in the insets of (a), (b), (f), and (g). The bottom scale bars apply to all super-resolution images in (a)−(d) and (f)−(i). (e, j) CBC scores for APF (green) and furfuryl alcohol (orange) bursts within the nanowire regions. Segments of other nanowires are seen in each super-resolution image. Only fluorescence bursts detected within the white outlines are included in (e) and (j).

when dimethyl sulfoxide (DMSO) was added to the solution of APF. DMSO has been previously shown to act as a scavenger for ·OH radicals.[35,42] Similar to the ensemble studies, very few fluorescence bursts (a number comparable to a blank sample) were observed for nanowires treated with H_2O_2 to remove oxygen vacancies. Under TIRF excitation, the generation of ·OH radicals in solution using the Fenton reaction (i.e., H_2O_2 and $Fe(ClO_4)_2$) did not produce fluorescence bursts, showing that the activation of APF by ·OH radicals occurs on the surface of the nanowires. Finally, simply adding a solution of fluorescein (30 nM in phosphate buffer) to the nanowires did not produce fluorescence bursts, which indicates that fluorescein (which has a higher density of negative charge than APF) does not bind as strongly to the $W_{18}O_{49}$ surface as APF. Thus, the turn-off events are attributed to either the desorption of fluorescein from the surface of a $W_{18}O_{49}$ nanowire or its decomposition into a nonfluorescent product.

By localizing the positions of individual fluorescence bursts collected over 1500−2500 frames (50 ms exposure), we acquired activity maps for single $W_{18}O_{49}$ nanowires with a localization precision of 22 nm (see Figure S28c for a histogram of the localization precision). The number of fluorescence bursts localized per nanowire ranged from 130 to 4000 among the 35 nanowires analyzed for this reaction. We did not observe any obvious correlation between morphological irregularities in the nanowires imaged by electron microscopy and the variations in activity imaged by single-molecule fluorescence (Figure S30). Furthermore, we kept the imaging short (typically below 5 min) to avoid photodegradation of the nanowires. Under the same illumination conditions used for single-molecule fluorescence (405 and 488 nm laser, buffer solution added), thin films of the nanowires showed no obvious structural changes after 5 min of irradiation, as evidenced by XPS and Raman spectroscopy (see Figures S11 and S12). However, we did observe loss of crystallinity in the nanowires after 30 min of irradiation. While catalytically active sites, such as oxygen vacancies, may diffuse during the time course of these experiments, their diffusion coefficients are too low to observe their mobility over this time period.[49,50] Figure 3c shows the activity map for photocatalytic ·OH radical generation of a representative nanowire, where the color scale indicates the number of fluorescence bursts detected in each accumulation bin (120 × 120 nm^2). Significant variations in activity are seen along the $W_{18}O_{49}$ nanowire, and similar variations were observed for all 35 nanowires imaged (see Figures S26 and S31−S33 in the Supporting Information for additional examples).

Tungsten oxide has been used as a solid-acid catalyst, similar to zeolites, due to the presence of both surface oxygen vacancies (Figure 1c, top), which act as Lewis acid sites, and surface hydroxyl groups (Figure 1c, bottom), which act as Bronsted acid sites.[11,51,52] Fourier-transform infrared spectroscopy (FT-IR) of chemically adsorbed pyridine indicated that dry powders of the $W_{18}O_{49}$ nanowires possessed both Lewis and Bronsted acid sites (Figure S10 and Table S4).[52] Bulk titration of acid sites in the presence or absence of 2,6-dimethylpyridine to selectively poison Bronsted sites gave concentrations of 0.305 mmol of Bronsted sites and 0.110 mmol of Lewis sites per gram of tungsten oxide (see the Supporting Information for further experimental details).[53−56] However, our single-molecule studies were conducted in an aqueous solution of phosphate buffer at pH 7.4. At this pH, hydroxyl groups at the surface of the nanowires are expected to be deprotonated due to the strong acidity of tungsten oxide (pH 0.43 at the point of zero charge), leading to a negative surface charge on the nanowires.[57] Consistent with this expectation, zeta potential measurements gave a value of −44.9 ± 0.3 mV (average ± first standard deviation from three measurements) when the nanowires were dispersed in a buffer solution at pH 7.4.

We next selected furfuryl alcohol as a probe molecule that can undergo acid-catalyzed condensation to generate fluorescent oligomers (Figure 2c).[33,58] The formation mechanism

https://dx.doi.org/10.1021/acscatal.9b04481
ACS Catal. 2020, 10, 2088−2099

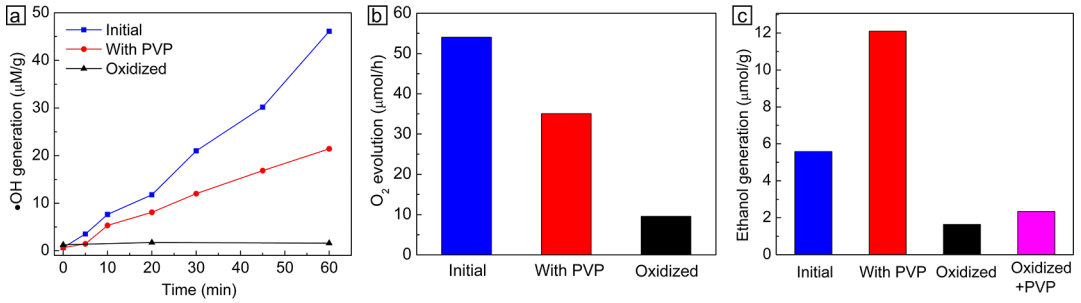

Figure 5. Ensemble catalytic activity of $W_{18}O_{49}$ nanowires. (a) Rate of photocatalytic ·OH generation for the initial $W_{18}O_{49}$ nanowires (blue squares), oxidized nanowires (black triangles), and PVP-functionalized nanowires (red circles) as measured by the reaction between ·OH and coumarin to produce fluorescent umbelliferone. (b) Rate of O_2 evolution for different nanowire samples during photocatalytic H_2O oxidation. (c) Amount of ethanol produced by different nanowire samples after the acid-catalyzed condensation of ethyl acetate for 24 h.

of fluorescent oligomers using both Lewis and Bronsted acids to catalyze this reaction has been previously described,[59,60] and tungsten oxide powders have been shown to catalyze the condensation of furfuryl alcohol.[58] Similar to the conditions used for APF, only Lewis acid sites are expected to be active in the as-synthesized $W_{18}O_{49}$ nanowires as surface hydroxyl groups will be deprotonated at pH 7.4. As this reaction does not require photoexcitation of the nanowires, TIRF excitation with a 561 nm laser (i.e., below the band gap energy of $W_{18}O_{49}$) was used to detect the oligomeric products. After addition of furfuryl alcohol, video recordings showed fluorescence intensity bursts similar to the case of APF (Figure S29a). These intensity bursts were not observed on blank coverslips in the same solution (Figure S25). Figure 3e shows a representative activity map, revealing that the $W_{18}O_{49}$ nanowires also displayed variations in activity along their length for this acid-catalyzed reaction. Similar variations in activity were observed for all 35 nanowires imaged using furfuryl alcohol as a probe molecule (see Figures S26 and S31−S33 for additional examples).

Coordinate-Based Colocalization. To directly correlate the active regions for photocatalytic ·OH radical generation with the distribution of Lewis acid sites, we sequentially performed single-molecule imaging with both APF and furfuryl alcohol as probe molecules on the same $W_{18}O_{49}$ nanowires (Figure 4a,f for APF and Figure 4b,g for furfuryl alcohol). Control experiments showed that APF used in the first round of imaging did not lead to fluorescence contamination during sequential imaging with the furfuryl alcohol probe (see Figure S34, Supporting Information, for further discussion). We used a coordinate-based colocalization (CBC) algorithm[61] to quantify the spatial correlation of each fluorescence burst from the two probes, yielding a value ranging from −1 for anticorrelated distributions, through 0 for random, to +1 for perfectly correlated distributions. The colocalization maps (Figure 4c,d,h,i) and the distribution of the CBC score across both nanowires (Figure 4e,j) show that the regions of each nanowire that are more active for generating ·OH radicals are also more active for the condensation of furfuryl alcohol. Figures S31−S33 provide additional examples of this colocalization analysis performed on the initial $W_{18}O_{49}$ nanowires. CBC analysis of 33 nanowires shows a high degree of colocalization between the two fluorogenic probes. Thus, not only is the catalytic activity heterogeneous along the lengths of individual nanowires, but also, to a large extent, the same segments within each nanowire are active for both reactions. The number of active regions along each nanowire is much lower than the bulk concentration of oxygen vacancies determined by acid titration, suggesting that clusters of vacancies rather than isolated defects are responsible for higher activity. Evidence that the crystallinity of the nanowires varies along their length comes from HRTEM images of different segments of the same nanowire (Figure S2).

As regions containing surface oxygen vacancies (i.e., Lewis acid sites) are active for both hydroxyl radical generation and furfuryl alcohol condensation, changing the availability of these sites should alter the catalytic activity of the nanowires. On the other hand, the availability of Bronsted acid sites should affect only the condensation reaction. To test this hypothesis, we applied different chemical modifications to the $W_{18}O_{49}$ nanowires and measured their resulting photocatalytic activity at both the ensemble and single-particle levels. We first oxidized the $W_{18}O_{49}$ nanowires using H_2O_2 to remove oxygen vacancies, similar to a previous report.[7] The X-ray diffraction pattern of the oxidized $W_{18}O_{49}$ nanowires was indistinguishable from the original pattern (Figure S5). However, the diffuse reflectance spectrum (Figure S4) of the oxidized nanowires showed significantly reduced absorption at long wavelengths (600 to 2000 nm). XPS showed both a decrease in the intensity of peaks corresponding to W^{4+} and W^{5+} and a decrease in surface-adsorbed oxygen species (Figures S8 and S9 and Table S3). Hydrogen peroxide adsorbed on the surface of the nanowires was not detected by FT-IR spectroscopy (Figure S7). The FT-IR spectra measured for dry powders of the nanowires after pyridine adsorption showed a decrease in the intensity of the peaks corresponding to Lewis acid sites, while the peaks corresponding to Bronsted acid sites did not change significantly (Figure S10). The zeta potential after oxidation (−42.1 ± 7.32 mV) was similar to the nanowires before oxidation (−44.9 ± 0.3 mV), indicating that the density of deprotonated surface hydroxyl groups did not change significantly. Similarly, acid titration of the oxidized nanowires gave a slightly reduced concentration of Bronsted acid sites (0.229 mmol per gram of tungsten oxide) compared to the initial nanowires (0.305 mmol/g) but a significantly decreased concentration of Lewis acid sites (0.003 vs 0.110 mmol/g). Together, these results demonstrate that the oxidation of the $W_{18}O_{49}$ nanowires using H_2O_2 decreases both the concentration of oxygen vacancies and the availability of Lewis acid sites but does not significantly change the availability of Bronsted acid sites.

We next treated both the initial and oxidized $W_{18}O_{49}$ nanowires with polyvinylpyrrolidone (PVP), a polymeric surfactant frequently used in the synthesis and assembly of

https://dx.doi.org/10.1021/acscatal.9b04481
ACS Catal. 2020, 10, 2088−2099

metal and metal oxide nanoparticles.[62−64] PVP aids in the colloidal stability and dispersibility of metal oxide particles. Tungsten oxide nanowires with PVP on their surface have been used as photocatalysts and electrocatalysts,[65,66] but the effect of the PVP coating on their activity has not been studied. After functionalization, XPS of the nanowires showed an increase in the signal from surface-adsorbed oxygen species without significant changes in the distribution of oxidation states for tungsten (Figures S8 and S9 and Table S3). The FT-IR spectra of the PVP-functionalized nanowires after pyridine adsorption displayed weaker and broader peaks for both Bronsted acid and Lewis acid sites (Figure S10 and Table S4), indicating that PVP was bound to both sites. In aqueous solution, the binding of PVP to surface hydroxyl groups can suppress deprotonation of the Bronsted acid sites. Evidence for this suppression is provided by differences in the zeta potential of the two samples. While the zeta potential was between −42 and −45 mV for the initial and oxidized nanowires before PVP treatment, it dropped to −8.4 ± 0.7 mV (average ± first standard deviation from three measurements) for the initial nanowires and to −5.6 ± 5.6 mV for the oxidized nanowires after functionalization with PVP.

Both APF and coumarin were used as fluorogenic probes to measure the rates of photocatalytic hydroxyl radical generation (see the Supporting Information for further details) using dispersions of $W_{18}O_{49}$ nanowires in solution. Coumarin reacts with ·OH radicals to generate the highly fluorescent umbelliferone (Figure S17).[45,46] As shown in Figure 5a, the initial $W_{18}O_{49}$ nanowires produced ·OH radicals at a greater rate compared to the ones functionalized with PVP. Nanowires oxidized with H_2O_2 produced a negligible amount of ·OH radicals (see also Figures S16 and S19). Removing oxygen vacancies via thermal annealing of the nanowires in air also gave negligible activity for ·OH generation. We next tested the activity of the different nanowire samples for both photocatalytic water oxidation and the degradation of Rhodamine B as these reactions rely on the generation of ·OH radicals.[38,45−47] As shown in Figure 5b, the initial nanowires showed the highest rate of oxygen evolution. PVP treatment led to a moderate reduction in activity, and oxidizing the nanowires led to a significant reduction in their activity for water oxidation. Similar activity trends were observed for the photocatalytic degradation of Rhodamine B (Figures S20 and S21). These ensemble measurements show that oxygen vacancies are necessary for photocatalytic activity, in agreement with previous studies.[3−11,17−19]

Different mechanisms have been proposed to explain the increased photocatalytic activity for metal oxide nanocrystals containing oxygen vacancies. These mechanisms include changes in the electronic structure induced by oxygen vacancies that lead to the narrowing of the band gap,[4,10] absorption enhancement through the sub-band gap, free carrier absorption,[5,16] and the activation of molecules adsorbed onto metal ions exposed by oxygen vacancies.[7,10,11] The high degree of colocalization between ·OH radical generation and the presence of oxygen vacancies imaged by single-molecule fluorescence reveals that regions containing oxygen vacancies are active sites for water oxidation. Previous DFT calculations show that a H_2O molecule will preferentially bind to a tungsten ion exposed by an oxygen vacancy at the (001) surface of WO_3, which activates the H_2O molecule toward dissociation to H^+ and OH^-.[67−70] An adsorbed OH^- ion can then be oxidized to an ·OH radical using photoexcited holes in the metal oxide.[71] These previous computational studies examined the activation of water at isolated oxygen vacancies. Our results indicate that clusters of oxygen vacancies form the catalytically active regions along $W_{18}O_{49}$ nanowires.

While PVP lowered the activity of the nanowires for the photocatalytic reactions described above, it increased their activity for acid-catalyzed reactions not requiring photoexcitation. As the condensation of furfuryl alcohol produces a complex distribution of products,[59,60] we used the acid-catalyzed hydrolysis of ethyl acetate in aqueous solution to compare the activity of different nanowires.[72,73] Oxidized nanowires, in which Lewis acid sites had been removed, produced a lower amount of ethanol than the initial nanowires (Figure 5c). However, PVP functionalization increased the relative activity of both the initial and oxidized nanowires. To further examine the role of PVP in modifying the surface of the nanowires, we used DFT to calculate the binding energy of a PVP monomer to different surface sites of tungsten oxide (see the Supporting Information for details of the calculations). For ease of calculation, we used a slab of WO_3 exposing the (001) surface, similar to previous studies.[67−70,74] While the $W_{18}O_{49}$ structure is more complex, the (001) facets of both $W_{18}O_{49}$ and WO_3 contain W−O bonds normal to the surface, allowing us to look at the interaction of a PVP monomer unit to either a single oxygen vacancy (i.e., Lewis acid site) or a hydroxyl group (i.e., Bronsted acid site). The strongest binding interactions were found between the electron-donating atoms of the PVP monomer and Lewis acid sites (i.e., −2.1 eV for binding via the O atom of PVP and −1.9 eV for binding via the N atom; see Figure S23 and Table S2). The lower activity observed for PVP-treated nanowires in reactions requiring photocatalytic ·OH generation arises from competitive binding of the polymer to these surface sites. Hydrogen bonding of the PVP monomer to a surface hydroxyl group was also favorable (i.e., −0.9 eV for binding via the O atom of PVP and −0.8 eV for binding via the N atom). While the hydrogen bonding interaction was weaker than binding to an oxygen vacancy, it was stronger than the PVP monomer binding to a deprotonated hydroxyl group (i.e., −0.6 eV between the deprotonated surface O atom and the carbonyl C atom of PVP). Thus, hydrogen bonding of PVP to surface hydroxyl groups appears to suppress their deprotonation at neutral pH, which is supported by the lower surface charge observed for PVP-treated nanowires. Dynamic hydrogen bonding of monomer units along the PVP polymer would allow Bronsted acid sites to still be available for the acid-catalyzed condensation of ethyl acetate, consistent with the higher activity seen for PVP-treated nanowires. In the future, incorporating the effects of different configurations of PVP oligomers could provide more accurate estimates of PVP binding to different surface sites of tungsten oxide.[75,76]

The ensemble changes in photocatalytic activity described above arise from the activation or deactivation of different sites on the nanowires. We next conducted the same correlative, single-molecule imaging on PVP-functionalized $W_{18}O_{49}$ nanowires using both APF and furfuryl alcohol as probes. Figure 6a,b,f,g shows the activity maps for both ·OH radical generation and furfuryl alcohol condensation obtained by localizing all fluorescence bursts. While they are strongly correlated in the initial nanowires (Figure 4e,j), PVP treatment consistently reduced the correlations between APF and FA localizations (Figure 6c−e,h−j), as reflected by a broader range of CBC scores (see Figures S36 and S37 for additional

https://dx.doi.org/10.1021/acscatal.9b04481
ACS Catal. 2020, 10, 2088−2099

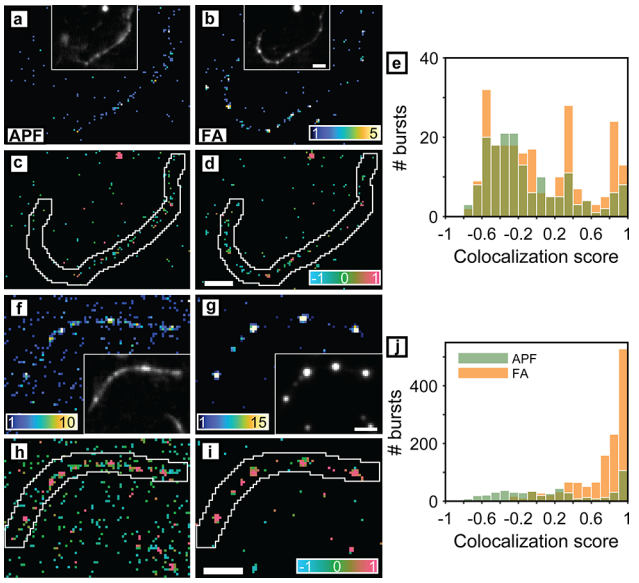

Figure 6. Colocalization of hydroxyl radical generation and acid sites for PVP-functionalized $W_{18}O_{49}$ nanowires. Super-resolution images of the nanowires using (a, f) APF as a probe to detect hydroxyl radicals and (b, g) furfuryl alcohol (FA) as a probe to identify Lewis and Bronsted acid sites. Color scale: number of fluorescence bursts per bin. Inset: diffraction-limited images of each imaging condition. Coordinate-based colocalization (CBC) of (c, h) APF and (d, i) furfuryl alcohol bursts. Color scale: median of the colocalization score in each bin, ranging from −1 for anticorrelated burst distributions, through 0 for random, to +1 for perfectly correlated burst distributions. White lines depict boundaries of the nanowire regions. All scale bars are 3 μm. The top scale bars apply to the diffraction-limited images in the insets of (a), (b), (f), and (g). The bottom scale bars apply to all super-resolution images in (a)−(d) and (f)−(i). (e, j) CBC scores for APF (green) and furfuryl alcohol (orange) bursts within the nanowire regions. Segments of other nanowires are seen in each super-resolution image. Only fluorescence bursts detected within the white outlines are included in (e) and (j).

examples). Accumulating the CBC scores across all 33 initial nanowires (Figure 7a,b) versus all 40 PVP-functionalized nanowires (Figure 7c,d) shows that PVP treatment simultaneously reduces the CBC scores for both species within each nanowire and increases the heterogeneity of CBC scores across nanowires (Figure 7e). Specifically, the per-nanowire CBC scores of APF (0.92 ± 0.08, average ± first standard deviation of median CBC score) and FA (0.89 ± 0.13) for the initial nanowires dramatically reduce to 0.19 ± 0.33 for APF and 0.54 ± 0.37 for FA for the PVP-functionalized ones (Figure 7e). Moreover, the heterogeneous effects of PVP functionalization are evidenced by the increased variation in CBC scores across nanowires after the treatment. We also attempted colocalization analysis for the oxidized nanowires. Similar to the low ensemble activity shown in Figure 5, the number of fluorescence bursts generated by the oxidized nanowires was reduced for both probe reactions to a level comparable to the background. Interestingly, after functionalizing the oxidized nanowires with PVP, the number of fluorescence bursts for the APF transformation was still low (Figure S35i), but the nanowires recovered their activity for FA condensation (Figure S35ii).

Negative CBC scores seen for localizations in the PVP-functionalized nanowires represent mutually exclusive sites for ·OH radical generation and furfuryl alcohol condensation. The photocatalytic generation of ·OH radicals at Lewis acid sites is inhibited after treating the nanowires with PVP. DFT calculations indicate that PVP inhibits activity by binding to the tungsten ions exposed by oxygen vacancies, thus blocking these sites for the adsorption of H_2O (Figure S23). This type of binding is supported by FT-IR spectroscopy (Figure S10a and Table S4) and the reduced ensemble photocatalytic activity for the PVP-functionalized nanowires seen in Figure 5. On the other hand, the binding of PVP to surface hydroxyl groups can suppress their deprotonation such that they become active for the acid-catalyzed condensation of both ethyl acetate and furfuryl alcohol. This mode of binding is also supported by FT-IR spectroscopy and the change in zeta potential after PVP functionalization. The intermediate binding energy calculated for hydrogen bonding between a PVP monomer and a surface hydroxyl group suggests that dynamic PVP binding in solution allows Bronsted acid sites to still protonate FA during the condensation reaction. Thus, we propose that the regions of the nanowire active for FA

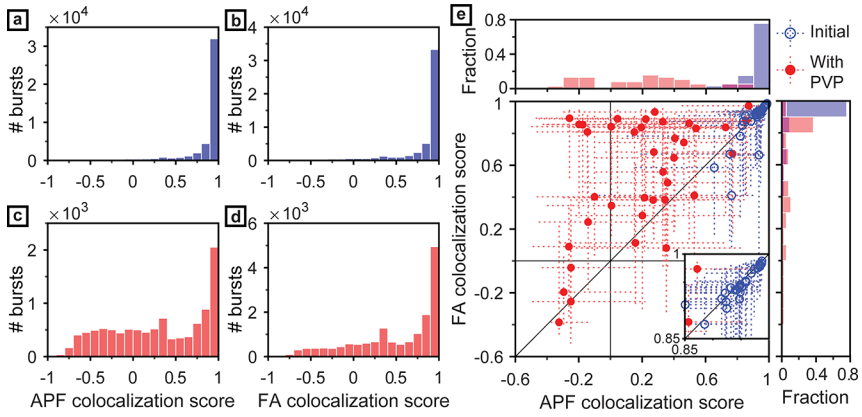

Figure 7. APF and furfuryl alcohol colocalization behavior on initial and PVP-functionalized $W_{18}O_{49}$ nanowires. Accumulated (a, c) APF and (b, d) furfuryl alcohol (FA) colocalization scores on 33 initial (blue) and 40 PVP-functionalized (red) nanowires. (e) Per-wire furfuryl alcohol versus APF colocalization scores for 73 initial and PVP-functionalized nanowires. Open and filled circles are the medians of the CBC scores across each nanowire. Dashed lines show CBC score ranges from 25th to 75th percentile of individual nanowires. Median APF (top) and furfuryl alcohol (right) CBC scores for each of the initial (blue) and PVP-functionalized (red) nanowires, where counts are given in fractions of the total population.

https://dx.doi.org/10.1021/acscatal.9b04481
ACS Catal. 2020, 10, 2088−2099

condensation, but not active for ·OH radical generation, expose Bronsted acid sites. Quantitative colocalization analysis of the two fluorogenic probes reveals this nanowire heterogeneity that cannot be observed at the ensemble level.

CONCLUSIONS

In summary, tungsten oxide nanowires show significant spatial variations in their catalytic activity. By spatially correlating the nanoscale regions that trigger two fluorogenic probe molecules, we demonstrate that segments containing clusters of oxygen vacancies are more active for generating hydroxyl radicals. While ensemble measurements can be used to measure average changes in the catalytic activity of a sample after chemical or thermal treatments, through this quantitative colocalization, we demonstrate how new sites become active in a photocatalyst after surface functionalization (i.e., Bronsted acid sites), while others are deactivated (i.e., metal ions bound by PVP) heterogeneously across nanowires. In the future, this method may be used to quantify the spatial correlation for other pairs of reactions, such as the locations of electron and hole extraction in nanostructured photoelectrodes.[37]

EXPERIMENTAL SECTION

Catalyst Preparation. $W_{18}O_{49}$ nanowires were prepared using a hydrothermal method. Tungsten chloride (0.040 g) and 1-butanol (40 mL) were mixed together, transferred to an acid digestion vessel, and heated at 453 K (180 °C) for 24 h. The product was washed repeatedly with ethanol and dried overnight in a vacuum oven. Oxidation of $W_{18}O_{49}$ nanowires was performed by mixing the $W_{18}O_{49}$ powder with hydrogen peroxide and 1 M sulfuric acid. The mixture was then washed repeatedly with ethanol and dried overnight. PVP functionalization of $W_{18}O_{49}$ nanowires was carried out by sonicating the $W_{18}O_{49}$ powder in an ethanolic solution of PVP. The mixture was then washed repeatedly with ethanol and dried overnight in a vacuum oven at 313 K (40 °C).

Ensemble Photocatalytic Reactions. The $W_{18}O_{49}$ nanowire powder was dispersed in an aqueous solution of phosphate buffer (pH 7.4) containing either APF (5 μM) and KIO_3 (10 μM), coumarin (0.1 μM) and KIO_3 (1 μM), or Rhodamine B (5 μM) and KIO_3 (1 μM). The suspension was irradiated with a 405 nm LED while stirring. Aliquots were collected periodically and centrifuged to remove the nanowires. Fluorescence spectra of the supernatants were then measured in quartz cuvettes using a Cary Eclipse spectrometer.

Photocatalytic Water Oxidation. The $W_{18}O_{49}$ nanowire powder (0.02 g) was dispersed in an aqueous solution of 0.1 M KIO_3. The suspension was then purged with argon for 30 min. Photocatalytic water oxidation was performed using a 350 W xenon lamp under argon flow and stirring of the reaction vessel. For each sample, the amount of O_2 produced was measured every 30 min using a Shimadzu GC-2014 gas chromatograph.

Acid-Catalyzed Hydrolysis of Ethyl Acetate. The $W_{18}O_{49}$ nanowire powder (5 mg) was dispersed in a solution of 1.9 mL of ethyl acetate and 0.1 mL of 0.1 M sodium phosphate buffer (pH 7). The suspension was sealed and stirred at 60 °C for 24 h. The amount of ethanol generated from each sample was then quantified using a Varian Unity Inova-600 NMR spectrometer.

Single-Molecule Fluorescence Microscopy with APF and Furfuryl Alcohol Probe Molecules. Glass microscope coverslips were cleaned, rinsed with DI water, and dried under N_2 flow before depositing the $W_{18}O_{49}$ nanowires. A well-dispersed suspension (30 μL) of the $W_{18}O_{49}$ nanowires in ethanol (10^{-4}%, w/v) was then spin-coated onto a cleaned coverslip. After drying under N_2 flow, the nanowire-coated coverslip was left in a vacuum oven at 10^{-2} atm and room temperature for 30 min to remove the residual solvent.

A Nikon N-STORM super-resolution microscopy system with a Nikon CFI-6-APO TIRF 1.49 NA, 100× oil-immersion objective lens was used for single-molecule fluorescence imaging. The incident angles of the laser illumination (405 and 488 nm or 561 nm) were adjusted to provide TIRF excitation at the coverslip surface. A quad-band filter set (405/488/561/647, CHROMA, TRF89902-NK) was used to collect emission from the fluorogenic probes, and an Andor iXon 897 electron-multiplying CCD with 160 nm effective pixel size was used for imaging. Image stacks of 2500 frames for APF oxidation and 1500 frames for the condensation of furfuryl alcohol were recorded at an exposure time of 50 ms. All measurements were carried out within 15 min after placing the coverslip on the microscope stage to limit system drift.

For imaging the oxidation of APF to produce fluorescein, a solution of 30 nM APF in phosphate buffer (pH 7.4) with 1 μM KIO_3 was dropped onto the coverslip. For this reaction, 405 and 488 nm lasers were used to photoexcite the $W_{18}O_{49}$ nanowires and fluorescein, respectively. For imaging the condensation of furfuryl alcohol, 100 μL of a solution of 10% furfuryl alcohol (v/v) in phosphate buffer was dropped onto the coverslip. A 561 nm laser was used to excite the fluorescent oligomers generated in this reaction. For both reactions, the solutions were purged with argon for 30 min before imaging. When imaging both reactions sequentially on the same set of $W_{18}O_{49}$ nanowires, the oxidation of APF was performed prior to the condensation of furfuryl alcohol to avoid contamination from the deposition of the polymeric product. In between imaging using the two probe molecules, the coverslip was repeatedly washed with phosphate buffer.

Image Analysis and Colocalization. All post-processing on the captured images was performed using MATLAB (MathWorks, R2019a) and ImageJ with the ThunderSTORM plugin.[77] Captured image stacks after offset subtraction using dark images were further background-corrected by a temporal quantile filter with 0.4 quantile and 200-frame sliding window (see Section 20 and Figure S24, Supporting Information, for further details). Single-molecule bursts in the corrected images were localized by using ThunderSTORM with default settings and custom camera parameters. Only localizations of single molecules with acceptable widths of the fitted point spread function (80 nm < σ < 220 nm) were retained for the following process. Detected photons per localization were obtained by summing up all photons within a region (5 × 5 pixels) centered at the localized positions. The estimated localization precision was calculated based on the photons detected and the estimated background, as previously described.[78] Localized single-molecule positions in each frame were grouped across consecutive frames to count intensity "bursts" of probe molecules on the nanowires (Section 21 and Figures S28 and S29, Supporting Information). Two-dimensional nanowire activation maps were then visualized by binning all single-molecule bursts within 120 × 120 nm^2 bins. Colocalization of APF and furfuryl alcohol super-resolution images was performed using coordinate-based colocalization (CBC) analysis.[61] First, system drift caused by the washing procedure

https://dx.doi.org/10.1021/acscatal.9b04481
ACS Catal. 2020, 10, 2088−2099

in-between APF and furfuryl alcohol imaging was estimated and removed by measuring shifts in the peaks of the cross-correlation between the diffraction-limited images of the two probes. CBC analysis calculates the colocalization between two super-resolution datasets directly using the localized coordinates of each molecule instead of the pixelized super-resolution reconstructions. Specifically, the spatial density surrounding each burst in the APF dataset was calculated from the neighboring bursts in both the APF and furfuryl alcohol datasets within discs of radius r (from 50 to 500 nm in 50 nm steps). The ordered-rank correlation coefficient is calculated using the two sets of the density distributions. Each coefficient was scaled by a weighting factor, depending on the distance to the nearest neighbor, to eliminate false-positive colocalizations for bursts whose nearest neighbor is far away. The final value was assigned as the colocalization (CBC) score of each burst in the APF dataset, and scores for each burst in the furfuryl alcohol dataset were calculated similarly. Colocalization scores vary from −1, representing perfectly excluded (anticorrelated) localizations, to +1 for perfectly colocalized localizations.

■ ASSOCIATED CONTENT

Supporting Information

The Supporting Information is available free of charge at https://pubs.acs.org/doi/10.1021/acscatal.9b04481.

Additional experimental details on the synthesis of tungsten oxide nanowires, their oxidation, PVP functionalization, and photoirradiation; additional details on methods used to characterize the structure and morphology of the nanowires; methods used to characterize ensemble catalytic activity; preparation of samples and instrumentation for single-molecule fluorescence microscopy; analysis and processing of super-resolution images and colocalization analysis; computational methods; supporting tables detailing the measurement conditions used for ensemble fluorescence microscopy; binding energies and bond lengths for a PVP monomer adsorbed onto different sites of tungsten oxide; electron binding energies measured from XPS; peak positions measured from FT-IR; the burst number, photon count, and on-time measurement for different nanowires using single-molecule fluorescence microscopy; supporting figures providing characterization of different nanowire samples by XRD, XPS, TEM, absorption spectroscopy, FT-IR spectroscopy, and Raman spectroscopy; ensemble fluorescence spectra for different photocatalytic transformations; schemes for different reactions catalyzed by tungsten oxide nanowires; calculated binding configurations of a PVP monomer to tungsten oxide; statistics showing the residual background photons after temporal quantile filtering; additional super-resolution images of tungsten oxide nanowires; region-of-interest selection for extracting single-molecule bursts; quantitative characterization of APF and furfuryl alcohol blinking events; colocalization analysis of additional nanowires; and correlation between SEM and fluorescence microscopy images (PDF)

■ AUTHOR INFORMATION

Corresponding Authors

Matthew D. Lew − *Department of Electrical and Systems Engineering and Institute of Materials Science & Engineering, Washington University, St. Louis, Missouri 63130, United States;* orcid.org/0000-0002-5614-3292; Email: mdlew@wustl.edu

Bryce Sadtler − *Department of Chemistry and Institute of Materials Science & Engineering, Washington University, St. Louis, Missouri 63130, United States;* orcid.org/0000-0003-4860-501X; Email: sadtler@wustl.edu

Other Authors

Meikun Shen − *Department of Chemistry, Washington University, St. Louis, Missouri 63130, United States*

Tianben Ding − *Department of Electrical and Systems Engineering, Washington University, St. Louis, Missouri 63130, United States;* orcid.org/0000-0003-0710-2344

Steven T. Hartman − *Institute of Materials Science & Engineering, Washington University, St. Louis, Missouri 63130, United States*

Fudong Wang − *Department of Chemistry, Washington University, St. Louis, Missouri 63130, United States;* orcid.org/0000-0003-2914-1360

Christina Krucylak − *Department of Chemistry, Washington University, St. Louis, Missouri 63130, United States*

Zheyu Wang − *Institute of Materials Science & Engineering, Washington University, St. Louis, Missouri 63130, United States*

Che Tan − *Department of Energy, Environmental & Chemical Engineering, Washington University, St. Louis, Missouri 63130, United States*

Bo Yin − *Institute of Materials Science & Engineering, Washington University, St. Louis, Missouri 63130, United States*

Rohan Mishra − *Institute of Materials Science & Engineering and Department of Mechanical Engineering and Materials Science, Washington University, St. Louis, Missouri 63130, United States;* orcid.org/0000-0003-1261-0087

Complete contact information is available at: https://pubs.acs.org/10.1021/acscatal.9b04481

Author Contributions

#M.S. and T.D. contributed equally to this work.

Notes

The authors declare no competing financial interest.

■ ACKNOWLEDGMENTS

This material is based on work supported by the National Science Foundation under grant no. CHE-1753344 to B.S. and under grant no. ECCS-1653777 to M.D.L. Acknowledgment is made to the donors of the American Chemical Society Petroleum Research Fund for partial support of this research (award #PRF58165-DNI10). B.S. and M.D.L acknowledge support from the International Center for Energy, Environment and Sustainability (InCEES) at Washington University. Computational resources were provided by the Extreme Science and Engineering Discovery Environment (XSEDE), which is supported by NSF grants ACI-1053575 and ACI-1548562. S.T.H. and R.M. acknowledge support from the NSF under grant no. DMREF CBET-1729787. Electron microscopy and X-ray photoelectron spectroscopy were performed at the Institute of Materials Science & Engineering at Washington University. X-ray diffraction was performed in the Department

of Earth and Planetary Sciences at Washington University. Zeta potential measurements were performed at the Nano Research Facility at Washington University. The authors thank S. Singamaneni for the use of his Raman spectrometer, B. Wieliczka and R. Loomis for the use of their absorption spectrometer, J. Lu for the helpful discussion, and O. Zhang for the technical assistance.

REFERENCES

(1) Xie, Y. P.; Liu, G.; Yin, L.; Cheng, H.-M. Crystal Facet-Dependent Photocatalytic Oxidation and Reduction Reactivity of Monoclinic WO_3 for Solar Energy Conversion. *J. Mater. Chem.* **2012**, *22*, 6746−6751.

(2) Li, R.; Han, H.; Zhang, F.; Wang, D.; Li, C. Highly Efficient Photocatalysts Constructed by Rational Assembly of Dual-Cocatalysts Separately on Different Facets of $BiVO_4$. *Energy Environ. Sci.* **2014**, *7*, 1369−1376.

(3) Chen, X.; Liu, L.; Yu, P. Y.; Mao, S. S. Increasing Solar Absorption for Photocatalysis with Black Hydrogenated Titanium Dioxide Nanocrystals. *Science* **2011**, *331*, 746−750.

(4) Lei, F.; Sun, Y.; Liu, K.; Gao, S.; Liang, L.; Pan, B.; Xie, Y. Oxygen Vacancies Confined in Ultrathin Indium Oxide Porous Sheets for Promoted Visible-Light Water Splitting. *J. Am. Chem. Soc.* **2014**, *136*, 6826−6829.

(5) Yan, J.; Wang, T.; Wu, G.; Dai, W.; Guan, N.; Li, L.; Gong, J. Tungsten Oxide Single Crystal Nanosheets for Enhanced Multichannel Solar Light Harvesting. *Adv. Mater.* **2015**, *27*, 1580−1586.

(6) Huang, Z.-F.; Song, J.; Pan, L.; Zhang, X.; Wang, L.; Zou, J.-J. Tungsten Oxides for Photocatalysis, Electrochemistry, and Phototherapy. *Adv. Mater.* **2015**, *27*, 5309−5327.

(7) Xi, G.; Ouyang, S.; Li, P.; Ye, J.; Ma, Q.; Su, N.; Bai, H.; Wang, C. Ultrathin $W_{18}O_{49}$ Nanowires with Diameters Below 1 nm: Synthesis, Near-Infrared Absorption, Photoluminescence, and Photochemical Reduction of Carbon Dioxide. *Angew. Chem., Int. Ed.* **2012**, *51*, 2395−2399.

(8) Chen, X.; Zhou, Y.; Liu, Q.; Li, Z.; Liu, J.; Zou, Z. Ultrathin, Single-Crystal WO_3 Nanosheets by Two-Dimensional Oriented Attachment toward Enhanced Photocatalystic Reduction of CO_2 into Hydrocarbon Fuels under Visible Light. *ACS Appl. Mater. Interfaces* **2012**, *4*, 3372−3377.

(9) Liang, L.; Li, X.; Sun, Y.; Tan, Y.; Jiao, X.; Ju, H.; Qi, Z.; Zhu, J.; Xie, Y. Infrared Light-Driven CO_2 Overall Splitting at Room Temperature. *Joule* **2018**, *2*, 1004−1016.

(10) Zhang, N.; Li, X.; Ye, H.; Chen, S.; Ju, H.; Liu, D.; Lin, Y.; Ye, W.; Wang, C.; Xu, Q.; Zhu, J.; Song, L.; Jiang, J.; Xiong, Y. Oxide Defect Engineering Enables to Couple Solar Energy into Oxygen Activation. *J. Am. Chem. Soc.* **2016**, *138*, 8928−8935.

(11) Zhang, N.; Li, X.; Liu, Y.; Long, R.; Li, M.; Chen, S.; Qi, Z.; Wang, C.; Song, L.; Jiang, J.; Xiong, Y. Defective Tungsten Oxide Hydrate Nanosheets for Boosting Aerobic Coupling of Amines: Synergistic Catalysis by Oxygen Vacancies and Brønsted Acid Sites. *Small* **2017**, *13*, 1701354.

(12) Villa, K.; Murcia-López, S.; Andreu, T.; Morante, J. R. Mesoporous WO_3 Photocatalyst for the Partial Oxidation of Methane to Methanol Using Electron Scavengers. *Appl. Catal., B* **2015**, *163*, 150−155.

(13) Zhu, W.; Shen, M.; Fan, G.; Yang, A.; Meyer, J. R.; Ou, Y.; Yin, B.; Fortner, J.; Foston, M.; Li, Z.; Zou, Z.; Sadtler, B. Facet-Dependent Enhancement in the Activity of Bismuth Vanadate Microcrystals for the Photocatalytic Conversion of Methane to Methanol. *ACS Appl. Nano Mater.* **2018**, *1*, 6683−6691.

(14) Pala, R. A.; Leenheer, A. J.; Lichterman, M.; Atwater, H. A.; Lewis, N. S. Measurement of Minority-Carrier Diffusion Lengths Using Wedge-Shaped Semiconductor Photoelectrodes. *Energy Environ. Sci.* **2014**, *7*, 3424−3430.

(15) Abdi, F. F.; Savenije, T. J.; May, M. M.; Dam, B.; van de Krol, R. The Origin of Slow Carrier Transport in $BiVO_4$Thin Film Photoanodes: A Time-Resolved Microwave Conductivity Study. *J. Phys. Chem. Lett.* **2013**, *4*, 2752−2757.

(16) Cheng, H.; Kamegawa, T.; Mori, K.; Yamashita, H. Surfactant-Free Nonaqueous Synthesis of Plasmonic Molybdenum Oxide Nanosheets with Enhanced Catalytic Activity for Hydrogen Generation from Ammonia Borane under Visible Light. *Angew. Chem., Int. Ed.* **2014**, *53*, 2910−2914.

(17) Gordon, T. R.; Cargnello, M.; Paik, T.; Mangolini, F.; Weber, R. T.; Fornasiero, P.; Murray, C. B. Nonaqueous Synthesis of TiO_2 Nanocrystals Using TiF_4 to Engineer Morphology, Oxygen Vacancy Concentration, and Photocatalytic Activity. *J. Am. Chem. Soc.* **2012**, *134*, 6751−6761.

(18) Wang, J.; Wang, Z.; Huang, B.; Ma, Y.; Liu, Y.; Qin, X.; Zhang, X.; Dai, Y. Oxygen Vacancy Induced Band-Gap Narrowing and Enhanced Visible Light Photocatalytic Activity of ZnO. *ACS Appl. Mater. Interfaces* **2012**, *4*, 4024−4030.

(19) Zhang, N.; Jalil, A.; Wu, D.; Chen, S.; Liu, Y.; Gao, C.; Ye, W.; Qi, Z.; Ju, H.; Wang, C.; Wu, X.; Song, L.; Zhu, J.; Xiong, Y. Refining Defect States in $W_{18}O_{49}$ by Mo Doping: A Strategy for Tuning N_2 Activation Towards Solar-Driven Nitrogen Fixation. *J. Am. Chem. Soc.* **2018**, *140*, 9434−9443.

(20) Zhao, Y.; Balasubramanyam, S.; Sinha, R.; Lavrijsen, R.; Verheijen, M. A.; Bol, A. A.; Bieberle-Hütter, A. Physical and Chemical Defects in WO_3 Thin Films and Their Impact on Photoelectrochemical Water Splitting. *ACS Appl. Energy Mater.* **2018**, *1*, 5887−5895.

(21) Manthiram, K.; Alivisatos, A. P. Tunable Localized Surface Plasmon Resonances in Tungsten Oxide Nanocrystals. *J. Am. Chem. Soc.* **2012**, *134*, 3995−3998.

(22) Xu, W.; Kong, J. S.; Yeh, Y.-T. E.; Chen, P. Single-Molecule Nanocatalysis Reveals Heterogeneous Reaction Pathways and Catalytic Dynamics. *Nat. Mater.* **2008**, *7*, 992−996.

(23) Zhou, X.; Andoy, N. M.; Liu, G.; Choudhary, E.; Han, K.-S.; Shen, H.; Chen, P. Quantitative Super-Resolution Imaging Uncovers Reactivity Patterns on Single Nanocatalysts. *Nat. Nanotechnol.* **2012**, *7*, 237−241.

(24) Andoy, N. M.; Zhou, X.; Choudhary, E.; Shen, H.; Liu, G.; Chen, P. Single-Molecule Catalysis Mapping Quantifies Site-Specific Activity and Uncovers Radial Activity Gradient on Single 2D Nanocrystals. *J. Am. Chem. Soc.* **2013**, *135*, 1845−1852.

(25) Zhou, X.; Choudhary, E.; Andoy, N. M.; Zou, N.; Chen, P. Scalable Parallel Screening of Catalyst Activity at the Single-Particle Level and Subdiffraction Resolution. *ACS Catal.* **2013**, *3*, 1448−1453.

(26) Du, Y.; He, X.; Zhan, Y.; Li, S.; Shen, Y.; Ning, F.; Yan, L.; Zhou, X. Imaging the Site-Specific Activity and Kinetics on a Single Nanomaterial by Microchamber Array. *ACS Catal.* **2017**, 3607−3614.

(27) Zou, N.; Chen, G.; Mao, X.; Shen, H.; Choudhary, E.; Zhou, X.; Chen, P. Imaging Catalytic Hotspots on Single Plasmonic Nanostructures Via Correlated Super-Resolution and Electron Microscopy. *ACS Nano* **2018**, *12*, 5570−5579.

(28) Wilson, A. J.; Willets, K. A. Visualizing Site-Specific Redox Potentials on the Surface of Plasmonic Nanoparticle Aggregates with Superlocalization SERS Microscopy. *Nano Lett.* **2014**, *14*, 939−945.

(29) Weber, M. L.; Wilson, A. J.; Willets, K. A. Characterizing the Spatial Dependence of Redox Chemistry on Plasmonic Nanoparticle Electrodes Using Correlated Super-Resolution Surface-Enhanced Raman Scattering Imaging and Electron Microscopy. *J. Phys. Chem. C* **2015**, *119*, 18591−18601.

(30) Chen, T.; Chen, S.; Song, P.; Zhang, Y.; Su, H.; Xu, W.; Zeng, J. Single-Molecule Nanocatalysis Reveals Facet-Dependent Catalytic Kinetics and Dynamics of Pallidium Nanoparticles. *ACS Catal.* **2017**, *7*, 2967−2972.

(31) Chen, T.; Dong, B.; Chen, K.; Zhao, F.; Cheng, X.; Ma, C.; Lee, S.; Zhang, P.; Kang, S. H.; Ha, J. W.; Xu, W.; Fang, N. Optical Super-Resolution Imaging of Surface Reactions. *Chem. Rev.* **2017**, *117*, 7510−7537.

(32) Roeffaers, M. B. J.; Sels, B. F.; Uji-i, H.; De Schryver, F. C.; Jacobs, P. A.; De Vos, D. E.; Hofkens, J. Spatially Resolved

https://dx.doi.org/10.1021/acscatal.9b04481
ACS Catal. 2020, 10, 2088−2099

Observation of Crystal-Face-Dependent Catalysis by Single Turnover Counting. *Nature* **2006**, *439*, 572−575.
(33) Roeffaers, M. B. J.; De Cremer, G.; Libeert, J.; Ameloot, R.; Dedecker, P.; Bons, A.-J.; Bückins, M.; Martens, J. A.; Sels, B. F.; De Vos, D. E.; Hofkens, J. Super-Resolution Reactivity Mapping of Nanostructured Catalyst Particles. *Angew. Chem., Int. Ed.* **2009**, *48*, 9285−9289.
(34) Han, R.; Ha, J. W.; Xiao, C.; Pei, Y.; Qi, Z.; Dong, B.; Bormann, N. L.; Huang, W.; Fang, N. Geometry-Assisted Three-Dimensional Superlocalization Imaging of Single-Molecule Catalysis on Modular Multilayer Nanocatalysts. *Angew. Chem., Int. Ed.* **2014**, *53*, 12865−12869.
(35) Xu, W.; Jain, P. K.; Beberwyck, B. J.; Alivisatos, A. P. Probing Redox Photocatalysis of Trapped Electrons and Holes on Single Sb-Doped Titania Nanorod Surfaces. *J. Am. Chem. Soc.* **2012**, *134*, 3946−3949.
(36) Tachikawa, T.; Yamashita, S.; Majima, T. Evidence for Crystal-Face-Dependent TiO_2 Photocatalysis from Single-Molecule Imaging and Kinetic Analysis. *J. Am. Chem. Soc.* **2011**, *133*, 7197−7204.
(37) Sambur, J. B.; Chen, T.-Y.; Choudhary, E.; Chen, G.; Nissen, E. J.; Thomas, E. M.; Zou, N.; Chen, P. Sub-Particle Reaction and Photocurrent Mapping to Optimize Catalyst-Modified Photoanodes. *Nature* **2016**, *530*, 77−80.
(38) Sambur, J. B.; Chen, P. Distinguishing Direct and Indirect Photoelectrocatalytic Oxidation Mechanisms Using Quantitative Single-Molecule Reaction Imaging and Photocurrent Measurements. *J. Phys. Chem. C* **2016**, *120*, 20668−20676.
(39) Mao, X.; Liu, C.; Hesari, M.; Zou, N.; Chen, P. Super-Resolution Imaging of Non-Fluorescent Reactions Via Competition. *Nat. Chem.* **2019**, *11*, 687−694.
(40) Hesari, M.; Mao, X.; Chen, P. Charge Carrier Activity on Single-Particle Photo(Electro)Catalysts: Toward Function in Solar Energy Conversion. *J. Am. Chem. Soc.* **2018**, *140*, 6729−6740.
(41) Tachikawa, T.; Yonezawa, T.; Majima, T. Super-Resolution Mapping of Reactive Sites on Titania-Based Nanoparticles with Water-Soluble Fluorogenic Probes. *ACS Nano* **2013**, *7*, 263−275.
(42) Ha, J. W.; Ruberu, T. P. A.; Han, R.; Dong, B.; Vela, J.; Fang, N. Super-Resolution Mapping of Photogenerated Electron and Hole Separation in Single Metal−Semiconductor Nanocatalysts. *J. Am. Chem. Soc.* **2014**, *136*, 1398−1408.
(43) Li, Y.; Bando, Y.; Golberg, D. Quasi-Aligned Single-Crystalline $W_{18}O_{49}$ Nanotubes and Nanowires. *Adv. Mater.* **2003**, *15*, 1294−1296.
(44) Guo, C.; Yin, S.; Yan, M.; Kobayashi, M.; Kakihana, M.; Sato, T. Morphology-Controlled Synthesis of $W_{18}O_{49}$ Nanostructures and Their Near-Infrared Absorption Properties. *Inorg. Chem.* **2012**, *51*, 4763−4771.
(45) Kim, J.; Lee, C. W.; Choi, W. Platinized WO_3 as an Environmental Photocatalyst That Generates OH Radicals under Visible Light. *Environ. Sci. Technol.* **2010**, *44*, 6849−6854.
(46) Zhang, J.; Nosaka, Y. Mechanism of the OH Radical Generation in Photocatalysis with TiO_2 of Different Crystalline Types. *J. Phys. Chem. C* **2014**, *118*, 10824−10832.
(47) Lops, C.; Ancona, A.; Di Cesare, K.; Dumontel, B.; Garino, N.; Canavese, G.; Hérnandez, S.; Cauda, V. Sonophotocatalytic Degradation Mechanisms of Rhodamine B Dye Via Radicals Generation by Micro- and Nano-Particles of ZnO. *Appl. Catal., B* **2019**, *243*, 629−640.
(48) Gomes, A.; Fernandes, E.; Lima, J. L. F. C. Fluorescence Probes Used for Detection of Reactive Oxygen Species. *J. Biochem. Biophys. Methods* **2005**, *65*, 45−80.
(49) Sikora, E.; Sikora, J.; Macdonald, D. D. A New Method for Estimating the Diffusivities of Vacancies in Passive Films. *Electrochim. Acta* **1996**, *41*, 783−789.
(50) Vázquez, G.; González, I. Diffusivity of Anion Vacancies in WO_3 Passive Films. *Electrochim. Acta* **2007**, *52*, 6771−6777.
(51) Barton, D. G.; Soled, S. L.; Iglesia, E. Solid Acid Catalysts Based on Supported Tungsten Oxides. *Top. Catal.* **1998**, *6*, 87−99.
(52) González, J.; Wang, J. A.; Chen, L. F.; Manríquez, M. E.; Dominguez, J. M. Structural Defects, Lewis Acidity, and Catalysis Properties of Mesostructured WO_3/SBA-15 Nanocatalysts. *J. Phys. Chem. C* **2017**, *121*, 23988−23999.
(53) Jacobs, P. A.; Heylen, C. F. Active Sites in Zeolites: III. Selective Poisoning of Bronsted Sites on Synthetic Y Zeolites. *J. Catal.* **1974**, *34*, 267−274.
(54) Oliviero, L.; Vimont, A.; Lavalley, J.-C.; Sarria, F. R.; Gaillard, M.; Maugé, F. 2,6-Dimethylpyridine as a Probe of the Strength of Brønsted Acid Sites: Study on Zeolites. Application to Alumina. *Phys. Chem. Chem. Phys.* **2005**, *7*, 1861−1869.
(55) Hong, J.; Djernes, K. E.; Lee, I.; Hooley, R. J.; Zaera, F. Heterogeneous Catalyst for the Selective Oxidation of Unactivated Hydrocarbons Based on a Tethered Metal-Coordinated Cavitand. *ACS Catal.* **2013**, *3*, 2154−2157.
(56) Weng, Z.; Yu, T.; Zaera, F. Synthesis of Solid Catalysts with Spatially Resolved Acidic and Basic Molecular Functionalities. *ACS Catal.* **2018**, *8*, 2870−2879.
(57) Xu, Y.; Schoonen, M. A. A. The Absolute Energy Positions of Conduction and Valence Bands of Selected Semiconducting Minerals. *Am. Mineral.* **2000**, *85*, 543−556.
(58) Chan, X.; Nan, W.; Mahajan, D.; Kim, T. Comprehensive Investigation of the Biomass Derived Furfuryl Alcohol Oligomer Formation over Tungsten Oxide Catalysts. *Catal. Commun.* **2015**, *72*, 11−15.
(59) Kim, T.; Assary, R. S.; Marshall, C. L.; Gosztola, D. J.; Curtiss, L. A.; Stair, P. C. Acid-Catalyzed Furfuryl Alcohol Polymerization: Characterizations of Molecular Structure and Thermodynamic Properties. *ChemCatChem* **2011**, *3*, 1451−1458.
(60) Choura, M.; Belgacem, N. M.; Gandini, A. Acid-Catalyzed Polycondensation of Furfuryl Alcohol: Mechanisms of Chromophore Formation and Cross-Linking. *Macromolecules* **1996**, *29*, 3839−3850.
(61) Malkusch, S.; Endesfelder, U.; Mondry, J.; Gelléri, M.; Verveer, P. J.; Heilemann, M. Coordinate-Based Colocalization Analysis of Single-Molecule Localization Microscopy Data. *Histochem. Cell Biol.* **2012**, *137*, 1−10.
(62) Pattanaik, M.; Bhaumik, S. K. Adsorption Behaviour of Polyvinyl Pyrrolidone on Oxide Surfaces. *Mater. Lett.* **2000**, *44*, 352−360.
(63) Koczkur, K. M.; Mourdikoudis, S.; Polavarapu, L.; Skrabalak, S. E. Polyvinylpyrrolidone (PVP) in Nanoparticle Synthesis. *Dalton Trans.* **2015**, *44*, 17883−17905.
(64) Wei, J.; Jiao, X.; Wang, T.; Chen, D. Electrospun Photochromic Hybrid Membranes for Flexible Rewritable Media. *ACS Appl. Mater. Interfaces* **2016**, *8*, 29713−29720.
(65) Zhou, X.; Qiu, Y.; Yu, J.; Yin, J.; Bai, X. High Electrochemical Activity from Hybrid Materials of Electrospun Tungsten Oxide Nanofibers and Carbon Black. *J. Mater. Sci.* **2012**, *47*, 6607−6613.
(66) Zhang, H.; Huang, C.; Tao, R.; Zhao, Y.; Chen, S.; Sun, Z.; Liu, Z. One-Pot Solvothermal Method to Synthesize Platinum/$W_{18}O_{49}$ Ultrafine Nanowires and Their Catalytic Performance. *J. Mater. Chem.* **2012**, *22*, 3354−3359.
(67) Ping, Y.; Sundararaman, R.; Goddard, W. A., III Solvation Effects on the Band Edge Positions of Photocatalysts from First Principles. *Phys. Chem. Chem. Phys.* **2015**, *17*, 30499−30509.
(68) Liu, L.; Lin, M.; Liu, Z.; Sun, H.; Zhao, X. Density Functional Theory Study of CO_2 and H_2O Adsorption on a Monoclinic WO_3(001) Surface. *Chem. Res. Chin. Univ.* **2017**, *33*, 255−260.
(69) Zhang, L.; Wen, B.; Zhu, Y.-N.; Chai, Z.; Chen, X.; Chen, M. First-Principles Calculations of Water Adsorption on Perfect and Defect WO_3(0 0 1). *Comput. Mater. Sci.* **2018**, *150*, 484−490.
(70) Kishore, R.; Cao, X.; Zhang, X.; Bieberle-Hütter, A. Electrochemical Water Oxidation on WO_3 Surfaces: A Density Functional Theory Study. *Catal. Today* **2019**, *321-322*, 94−99.
(71) Hu, J.; Zhao, X.; Chen, W.; Su, H.; Chen, Z. Theoretical Insight into the Mechanism of Photoelectrochemical Oxygen Evolution Reaction on $BiVO_4$ Anode with Oxygen Vacancy. *J. Phys. Chem. C* **2017**, *121*, 18702−18709.

https://dx.doi.org/10.1021/acscatal.9b04481
ACS Catal. 2020, 10, 2088−2099

(72) Nakato, T.; Kimura, M.; Nakata, S.-i.; Okuhara, T. Changes of Surface Properties and Water-Tolerant Catalytic Activity of Solid Acid $Cs_{2.5}H_{0.5}PW_{12}O_{40}$ in Water. *Langmuir* **1998**, *14*, 319−325.
(73) Koito, Y.; Rees, G. J.; Hanna, J. V.; Li, M. M. J.; Peng, Y.-K.; Puchtler, T.; Taylor, R.; Wang, T.; Kobayashi, H.; Teixeira, I. F.; Khan, M. A.; Kreissl, H. T.; Tsang, S. C. E. Structure−Activity Correlations for Brønsted Acid, Lewis Acid, and Photocatalyzed Reactions of Exfoliated Crystalline Niobium Oxides. *ChemCatChem* **2017**, *9*, 144−154.
(74) Albanese, E.; Di Valentin, C.; Pacchioni, G. H_2O Adsorption on WO_3 and WO_{3-x} (001) Surfaces. *ACS Appl. Mater. Interfaces* **2017**, *9*, 23212−23221.
(75) Zhou, Y.; Saidi, W. A.; Fichthorn, K. A. A Force Field for Describing the Polyvinylpyrrolidone-Mediated Solution-Phase Synthesis of Shape-Selective Ag Nanoparticles. *J. Phys. Chem. C* **2014**, *118*, 3366−3374.
(76) Liu, S.-H.; Saidi, W. A.; Zhou, Y.; Fichthorn, K. A. Synthesis of {111}-Faceted Au Nanocrystals Mediated by Polyvinylpyrrolidone: Insights from Density-Functional Theory and Molecular Dynamics. *J. Phys. Chem. C* **2015**, *119*, 11982−11990.
(77) Ovesný, M.; Křížek, P.; Borkovec, J.; Švindrych, Z.; Hagen, G. M. ThunderSTORM: A Comprehensive ImageJ Plug-in for PALM and STORM Data Analysis and Super-Resolution Imaging. *Bioinformatics* **2014**, *30*, 2389−2390.
(78) Rieger, B.; Stallinga, S. The Lateral and Axial Localization Uncertainty in Super-Resolution Light Microscopy. *ChemPhysChem* **2014**, *15*, 664−670.

https://dx.doi.org/10.1021/acscatal.9b04481
ACS Catal. 2020, 10, 2088−2099